論文 / 著書情報
Article / Book Information

Title	Polar metallic behavior of strained antiperovskites ACNi3 (A = Mg, Zn, and Cd) from first principles
Authors	Yasuhide Mochizuki, Yu Kumagai, Hirofumi Akamatsu, Fumiyasu Oba
Citation	Physical Review Materials, Vol. 2, Issue 12,
Pub. date	2018, 12
DOI	http://dx.doi.org/10.1103/PhysRevMaterials.2.125004
Creative Commons	See next page.

Polar metallic behavior of strained antiperovskites $ACNi_3$ (A = Mg, Zn, and Cd) from first principles

Yasuhide Mochizuki,[1,*] Yu Kumagai,[2] Hirofumi Akamatsu,[3] and Fumiyasu Oba[1,2,4]

[1]*Laboratory for Materials and Structures, Institute of Innovative Research, Tokyo Institute of Technology, Yokohama 226-8503, Japan*

[2]*Materials Research Center for Element Strategy, Tokyo Institute of Technology, Yokohama 226-8503, Japan*

[3]*Department of Applied Chemistry, Kyushu University, 744 Motooka, Fukuoka 819-0395, Japan*

[4]*Center for Materials Research by Information Integration, Research and Services Division of Materials Data and Integrated System, National Institute for Materials Science, Tsukuba 305-0047, Japan*

(Received 1 October 2018; published 26 December 2018)

Stable structures of metallic antiperovskites $ACNi_3$ (A = Mg, Zn, and Cd) under epitaxial strain are explored using first-principles lattice dynamics calculations. Although the ground states of $ACNi_3$ are cubic nonpolar phases without structural distortion, transitions to polar phases are predicted to arise in these compounds under compressive strain while maintaining metallic states. In particular, the polar phase of $MgCNi_3$ would be attainable with moderate strain of a few percent. The polar distortions are considered to be generated by the enhancement of the hybridization between C 2p and Ni 3d states, which is a mechanism analogous to that of the previously discovered polar metal $CeSiPt_3$.

DOI: 10.1103/PhysRevMaterials.2.125004

I. INTRODUCTION

Perovskite transition-metal oxides have been intensely studied from both fundamental and technological viewpoints because they exhibit diverse and fascinating phenomena such as ferroelectricity, ferromagnetism, piezoelectricity, and superconductivity. These physical properties are closely correlated to structural distortions such as rotation, tilting, and deformation of the oxygen-coordinated octahedra enclosing the transition metals, the instability of which strongly depends on external pressure and strain [1]. Recently, elastic strain engineering, in particular, of perovskite oxides, has attracted considerable attention not only for enhancing carrier mobility, catalytic activity, and the transition temperatures of superconductivity and ferroelectricity but also for generating ferroelectricity, ferromagnetism, and multiferroicity that are not realized in unstrained bulk states [2]. First-principles calculations are helpful for explaining or even predicting the strain effect; strain-induced ferroelectricity in $SrTiO_3$ [3] and multiferroicity in $BiFeO_3$ [4] and $EuTiO_3$ [5] are distinctive examples that have been realized using a combination of thin-films strain engineering and first-principles calculations [6].

Antiperovskites with AXM_3 formula (A = p-group elements and late transition metals, X = C, N, and O; M = transition metals and alkaline-earth metals) [Fig. 1(a)], especially their transition metal compounds with metallic behavior, have recently attracted broad interest because of their wide variety of intriguing physical properties such as superconductivity [7–12], magnetoresistance [13], magnetostriction [14], giant negative thermal expansion [15], topological insulating property [16], and Dirac semimetallic behavior [17,18]. In contrast to conventional perovskite oxides, most of the reported crystal structures are cubic without structural distortion [Table I]. Thus, as-yet-unreported physical properties are expected to be realized when structural distortions are introduced via epitaxial strain as in the perovskite oxides. Indeed, the fabrication of several antiperovskites epitaxial thin-film has been demonstrated [19–22].

In this study, we report our first-principles calculation results to reveal the ground-state crystal and electronic structures of antiperovskites $ACNi_3$ (A = Mg, Zn, and Cd) with and without strain. Among them, $MgCNi_3$ is a representative antiperovskite that has inspired researchers to explore the other antiperovskites [8–11,23–27]. We have found that in $MgCNi_3$, moderate compressive strain drives a nonpolar-to-polar phase transition while maintaining metallic behavior accompanied by the lattice distortion Γ_3^- mode [Fig. 1(b)], whereas the phase transition in $CdCNi_3$ requires large strain. Such "polar metals" or "ferroelectric-like metals" of strained $MgCNi_3$ and $CdCNi_3$ would provide a promising playground for intriguing physics [28,29]. However, an antipolar phase is predicted to be stable for $ZnCNi_3$. The feasibility of strained $MgCNi_3$ is demonstrated by comparing $BiFeO_3$ and $EuTiO_3$ in terms of the strain dependence of the total energies. Further, we compare these identified polar metals with the reported ones to unveil the mechanism behind the polar metallic behavior; notably, we find that the mechanism for $ACNi_3$ (A = Mg, Zn, and Cd) is analogous to that for the previously discovered polar metal $CeSiPt_3$ despite the significant dissimilarity in chemical composition.

II. COMPUTATIONAL DETAILS

Our first-principles calculations were carried out using the projector augmented-wave method (PAW) [40] and the

*mochizuki.y.af@m.titech.ac.jp

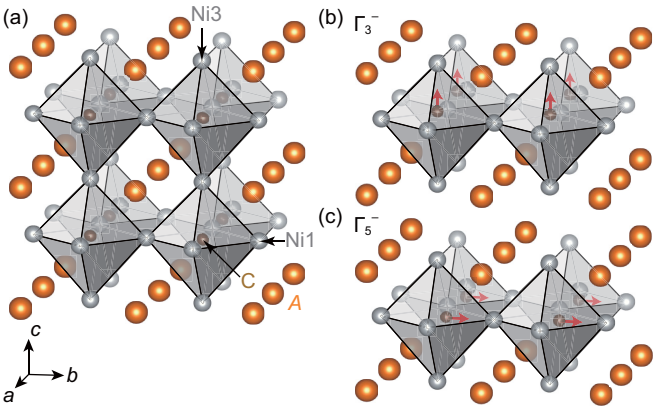

FIG. 1. Schematics of (a) the $2 \times 2 \times 2$ supercell of the $ACNi_3$ (A = Mg, Zn, and Cd) primitive cell, and the lattice distortion modes of the $P4/mmm$ structure that transform like irreducible representation (irrep) (b) Γ_3^- and (c) $\Gamma_5^-(a, 0)$, respectively. The apical Ni atoms along the in-plane and out-of-plane directions are denoted as Ni1 and Ni3, respectively.

PBEsol functional within the generalized gradient approximation [41] as implemented in the VASP code [42,43]. The on-site Hubbard U correction [44] was used for Fe $3d$ in $BiFeO_3$ and Eu $4f$ in $EuTiO_3$ with the effective U parameters of 3 and 6 eV, respectively. PAW data sets with radial cutoffs of 0.9, 0.8, 1.5, 1.3, 1.3, 1.3, 1.3, 1.3, 1.6, 1.3, 1.5, 1.5, and 1.6 Å for C, O, Mg, Si, Ti, Fe, Ni, Zn, Cd, Ce, Eu, Pt, and Bi, respectively, were used in conjunction with a cutoff energy of 550 eV for the plane-wave basis. The following valence electrons were considered: $3s$ for Mg; $3d$ and $4s$ for Ti, Fe, Ni, and Zn; $4d$ and $5s$ for Cd; $6s$ and $6p$ for Bi; $2s$ and $2p$ for C and O; $3s$ and $3p$ for Si; $4f$, $5p$, $5d$, and $6s$ for Ce and Eu; and $5d$ and $6s$ for Pt. The lattice constants and internal coordinates were optimized until the residual stress and forces converged down to 0.04 GPa and 10 meV/Å, respectively. The phonon band structures were derived from the calculated force constants using the PHONOPY code [45]. The symmetry of the parent structure without strain is $Pm\bar{3}m$ but reduced to $P4/mmm$ when in-plane [100] and [010] biaxial strain is applied. We used $2 \times 2 \times 2$ supercells that were constructed by expanding their primitive unit cells to explore the ground-state structures as illustrated in Fig. 1(a). $6 \times 6 \times 6$ and $12 \times 12 \times 12$ Γ-centered k-point meshes were used for the supercells and unit cells, respectively.

In our ground-state search, when imaginary modes were found, we distorted the structures following them and optimized their lattice constants and atomic coordinates in the same manner used in the previous reports [46–48]. This flow was iterated until all imaginary phonon modes disappeared. Symmetry mode analysis was performed using the AMPLIMODES code [49,50]. The chemical bonding analysis through crystal orbital Hamiltonian populations (COHPs) was performed using the LOBSTER code [51–55] and the Bader charges were calculated using the BADER code [56–59].

TABLE I. Space groups (SGs) for experimentally reported antiperovskites with formula AXM_3 (A = p-group elements and late transition metals; X = C, N, and O; M = transition metals and alkaline earth metals) at room temperature. The metallic and insulating behaviors are denoted in the parentheses as M and I, respectively.

Formula	SGs	Formula	SGs
$MgCNi_3$	$Pm\bar{3}m$ (M) [8]	$AlCNi_3$	$Pm\bar{3}m$ (M) [24]
$ZnCNi_3$	$Pm\bar{3}m$ (M) [23]	$GaCNi_3$	$Pm\bar{3}m$ (M) [25]
$CdCNi_3$	$Pm\bar{3}m$ (M) [9]	$InCNi_3$	$Pm\bar{3}m$ (M) [26]
$CuNNi_3$	$Pm\bar{3}m$ (M) [11]	$ZnNNi_3$	$Pm\bar{3}m$ (M) [10]
$CdNNi_3$	$Pm\bar{3}m$ (M) [27]	$InNNi_3$	$Pm\bar{3}m$ (M) [27]
$GaCMn_3$	$Pm\bar{3}m$ (M) [13]	$SnCMn_3$	$Pm\bar{3}m$ (M) [30]
$CuNMn_3$	$Pm\bar{3}m$ (M) [14,31]	$ZnNMn_3$	$Pm\bar{3}m$ (M) [32]
$AlNSc_3$	$Pm\bar{3}m$ (M) [33]	$InNSc_3$	$Pm\bar{3}m$ (M) [34]
$SnOCa_3$	$Pm\bar{3}m$ (M) [39]	$PbOCa_3$	$Pm\bar{3}m$ (M) [18]
$SnOSr_3$	$Pm\bar{3}m$ (M) [12]	$PbOSr_3$	$Pm\bar{3}m$ (M) [19]
$GeNCa_3$	$Pm\bar{3}m$ (M) [36]	$SnNCa_3$	$Pm\bar{3}m$ (M) [36]
$PbNCa_3$	$Pm\bar{3}m$ (M) [36]		
$AsNCa_3$	$Pnma$ (I) [36,37]		
$SbNCa_3$	$Pm\bar{3}m$ (I) [36]	$BiNCa_3$	$Pm\bar{3}m$ (I) [16,36]
$AsNMg_3$	$Pm\bar{3}m$ (I) [35]	$SbNMg_3$	$Pm\bar{3}m$ (I) [35]
$SbNSr_3$	$Pm\bar{3}m$ (I) [38]	$BiNSr_3$	$Pm\bar{3}m$ (I) [16,38]

III. RESULTS AND DISCUSSION

A. Ground-state crystal and electronic structure of bulk

It has been experimentally reported that $MgCNi_3$, $Zn_{1.2}C_{1.3}Ni_3$, and $Cd_{1.1}CNi_3$ exhibit Pauli paramagnetic behavior above 5 K, 2 K and approximately room temperature, respectively [8,9,23]. We observed that the structures of the unstrained bulk $MgCNi_3$, $ZnCNi_3$, and $CdCNi_3$ with space group $Pm\bar{3}m$ converge to nonmagnetic electronic states in spin-polarized calculations; these findings are consistent with the experiments. The calculated lattice constants for the $Pm\bar{3}m$ structures of $MgCNi_3$, $ZnCNi_3$, and $CdCNi_3$ (3.77, 3.72, and 3.81 Å, respectively) are close to the the experimental values of 3.81 [8], 3.66 [23], and 3.84 [9] Å, respectively. This tendency of the lattice constants can be explained using empirical atomic radii of 1.50, 1.35, and 1.55 Å for Mg, Zn, and Cd, respectively [60].

We then explored stable crystal structures for $MgCNi_3$, $ZnCNi_3$, and $CdCNi_3$ using lattice dynamics calculations. The phonon band structures of the parent $Pm\bar{3}m$ structures are shown in Figs. 2(a)–2(c). Note that we used the special points of the $P4/mmm$ symmetry [Fig. 2(d)] to compare the unstrained and strained states. Accordingly, the X and M points are equal to the Z and R points, respectively, in the $Pm\bar{3}m$ symmetry. For $MgCNi_3$ and $CdCNi_3$, no lattice instabilities are observed at the special points. In contrast, one imaginary phonon mode is found for $ZnCNi_3$, which transforms like irreducible representation (irrep) X_5^+ (see Fig. S1 of the Supplemental Material [61]). The relaxed structure after being displaced along the X_5^+ mode is dynamically stable with the $Cmcm$ symmetry. However, the total energy is only 1 meV/f.u. (formula unit) lower than that of the parent $Pm\bar{3}m$ structure, and the distortion is not significant.

The atom-projected local density of states (DOS) for the $Pm\bar{3}m$ structures in $MgCNi_3$, $ZnCNi_3$, and $CdCNi_3$ is described in Figs. 3(a)–3(c). A notable feature common to the three compounds is the sharp DOS just 0.05 eV below the Fermi level, which is mostly constructed from π^* orbitals

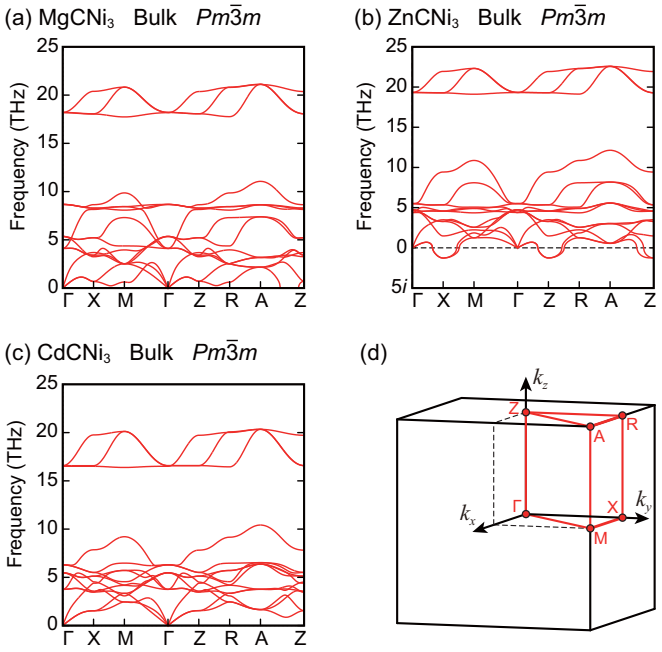

FIG. 2. Phonon band structures for the unstrained bulk parent $Pm\bar{3}m$ structures of (a) $MgCNi_3$, (b) $ZnCNi_3$, and (c) $CdCNi_3$. The relevant special points in the first Brillouin zone are represented using those of the $P4/mmm$ structure as shown in (d). Note that the range of the vertical axes lower than zero has imaginary units.

composed of C $2p$ and Ni $3d$, as will be discussed later. In $ZnCNi_3$ and $CdCNi_3$, the localized Zn $3d$ and Cd $4d$ DOS lies on approximately -7 and -9 eV, respectively. From the Bader charges summarized in Table II, one can see that all the A-site atoms and C atoms behave as cations and anions, respectively, whereas the Ni atoms are almost neutral but behave somewhat like anions (cations) in $MgCNi_3$ ($ZnCNi_3$ and $CdCNi_3$). This tendency is understood in terms of the Pauling's electronegativities of 1.31, 1.65, 1.69, 2.55, and 1.91 for Mg, Zn, Cd, C, and Ni, respectively [62]. The chemical trend of the charge for B-site atoms, i.e., that for C in *antiperovskites* $ACNi_3$ is in sharp contrast to that for conventional perovskites. In addition, the local DOS indicates that the Ni $3d$ states are mostly occupied while the Ni $4s$ states are partially occupied. Near the Fermi level between –4 and 4 eV, the local density

TABLE II. Bader charges for relevant phases in $MgCNi_3$, $ZnCNi_3$, and $CdCNi_3$. Ni1,2 and Ni3 indicate the apical Ni atoms in the in-plane and out-of-plane directions, respectively, as shown in Fig. 1(a).

$MgCNi_3$	Mg	C	Ni1,2	Ni3
$Pm\bar{3}m$ ($\epsilon_s = 0\%$)	+1.52	–1.03	–0.16	–0.16
$P4/mmm$ ($\epsilon_s = -5\%$)	+1.52	–0.92	–0.15	–0.30
$P4mm$ ($\epsilon_s = -5\%$)	+1.54	–1.01	–0.10	–0.33
$Cmm2$ ($\epsilon_s = -5\%$)	+1.54	–0.98	–0.13	–0.30
$ZnCNi_3$	Zn	C	Ni1,2	Ni3
$Pm\bar{3}m$ ($\epsilon_s = 0\%$)	+0.33	–0.91	+0.19	+0.19
$P4/mmm$ ($\epsilon_s = -5\%$)	+0.33	–0.79	+0.16	+0.13
$P4mm$ ($\epsilon_s = -5\%$)	+0.38	–0.86	+0.20	+0.08
$Pmn2_1$ ($\epsilon_s = -5\%$)	+0.35	–0.84	+0.18	+0.14
$CdCNi_3$	Cd	C	Ni1,2	Ni3
$Pm\bar{3}m$ ($\epsilon_s = 0\%$)	+0.18	–0.89	+0.24	+0.24
$P4/mmm$ ($\epsilon_s = -5\%$)	+0.22	–0.84	+0.22	+0.19
$P4mm$ ($\epsilon_s = -5\%$)	+0.29	–0.87	+0.22	+0.15

of states at the Ni site is much higher than that at the Mg, Zn, Cd, and C sites [Figs. 3(a)–3(c)].

B. Ground-state structures under biaxial strain

We then explored the ground-state structures under biaxial strain. We define epitaxial strain as $\epsilon_s = (a - a_0)/a_0$, where a_0 is the in-plane lattice constant of the unstrained bulk $Pm\bar{3}m$ structure. The ground-state structures were explored using phonon calculations under $\epsilon_s = \pm 5\%$, which are extreme conditions in experiments; for instance, the largest strain on $BiFeO_3$ was reported to be –6.6% [2]. In these calculations, we relaxed the out-of-plane lattice constant while fixing the in-plane one. Figure 4 shows the phonon band structures of the parent $P4/mmm$ phases and treelike line diagrams summarizing the structural search at $\epsilon_s = -5\%$; here we mostly focus on structure explorations under compressive strain as intriguing polar-metal phases are predicted to be stable. The results for tensile strain are discussed in the Supplemental Material [61].

$MgCNi_3$. Six imaginary phonon modes transforming like irreps Γ_3^-, X_2^-, X_2^+, X_3^+, M_5^+, and A_1^- are found at the special points; the structural evolution pathway, the space groups of

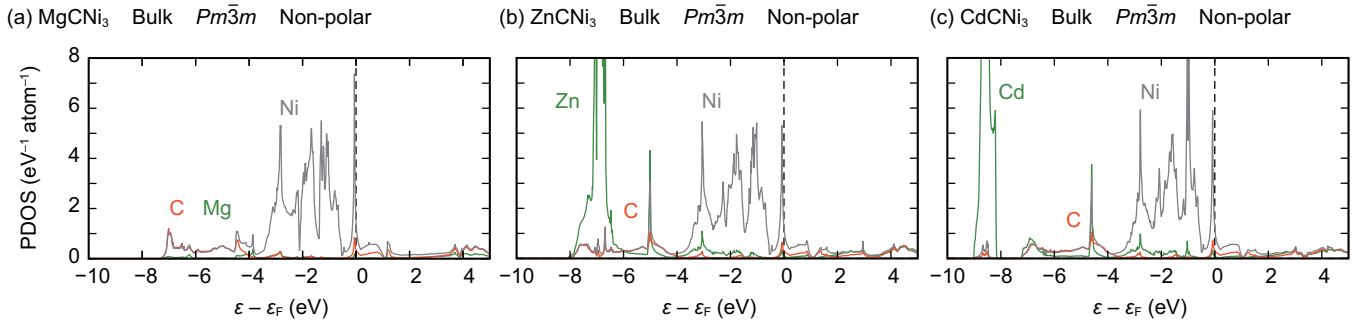

FIG. 3. Atom-projected local density of states for (a) $MgCNi_3$, (b) $ZnCNi_3$, and (c) $CdCNi_3$ in the unstrained bulk $Pm\bar{3}m$ structure. The vertical broken lines indicate the Fermi levels (ϵ_F). The green, red, and grey lines represent the DOS projected for A (A = Mg, Zn, and Cd), C, and Ni sites, respectively.

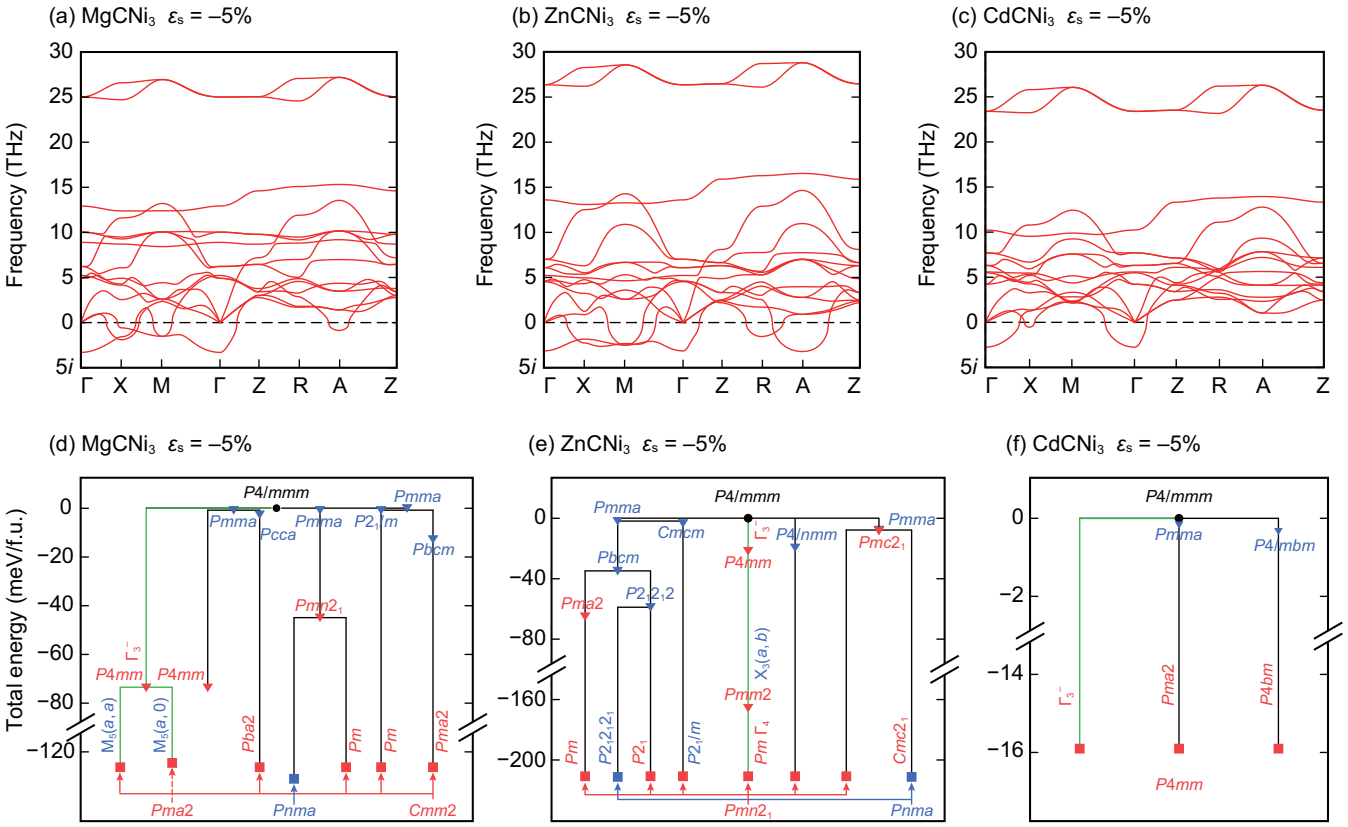

FIG. 4. Phonon band structures of the parent $P4/mmm$ structures for (a) $MgCNi_3$, (b) $ZnCNi_3$, and (c) $CdCNi_3$ and treelike line diagrams for (d) $MgCNi_3$, (e) $ZnCNi_3$, and (f) $CdCNi_3$ under 5% compressive strain. The green lines indicate the pathway explained in the main text. The red and blue text signifies polar and antipolar structures, respectively. Space groups denoted horizontally and vertically indicate relaxed and unrelaxed distorted structures following the relevant irreps, respectively. Note that the energy scales in (d–f) are different and the irreps are denoted only in the explained pathway.

the derived structures, and the relevant irreps are given in Fig. 4(d) and Table III. The $P4mm$ structure appears when atoms are displaced along the Γ_3^- phonon mode, which leads to a nonpolar-to-polar phase transition in the [001] direction as shown in Fig. 1(b). The $P4mm$ structure still has unstable phonon modes according to irreps $M_5(a,a)$ and $M_5(a,0)$, which generate two dynamically stable $Cmm2$ and $Pma2$ structures, respectively. There are four other routes that reach the $Cmm2$ structure, as illustrated in Fig 4(d). In addition, we found one more dynamically stable antipolar $Pnma$ structure (see Table S1 and Fig. S2 of the Supplemental Material [61]). Consequently, the $Pnma$ structure is found to be the most stable under 5% compressive strain with an energy difference between these three dynamically stable structures of less than only 6 meV/f.u. Meanwhile, as shown in Fig. 5(a), we found that the polar $Cmm2$ structure is stable under moderate compressive strain $-4.5\% < \epsilon_s < -2.8\%$. This finding is important as this amount of strain should be attainable in experiments.

TABLE III. Appearing space groups (SGs), space group numbers (SGs#), irreducible representations (irreps) of the $P4/mmm$ symmetry, and total energies in units of meV/f.u. with respect to those of the $P4/mmm$ structures (ΔE) for the polar structures of $MgCNi_3$, $ZnCNi_3$, and $CdCNi_3$ under 5% compressive strain.

SGs (SGs#)	Irreps	ΔE
$MgCNi_3$		
$P4mm$ (99)	Γ_3^-	–74
$Pma2$ (28)	$\Gamma_3^- \oplus M_5^-(a,0) \oplus M_5^+(a,0)$	–125
$Cmm2$ (35)	$\Gamma_3^- \oplus M_5^-(a,a) \oplus M_5^+(a,a)$	–126
$ZnCNi_3$		
$P4mm$ (99)	Γ_3^-	–22
$Pmm2$ (25)	$\Gamma_3^- \oplus M_3^+ \oplus X_3^+(a,b)$	–166
$Pmn2_1$ (31)	$\Gamma_5^-(a,0) \oplus M_3^+ \oplus X_3^+(a,b)$ $\oplus M_5^-(a,a) \oplus X_2^-(a,a)$	–211
$CdCNi_3$		
$P4mm$ (99)	Γ_3^-	–16

$ZnCNi_3$. Seven imaginary phonon modes transforming like irreps Γ_3^-, X_2^+, X_3^+, M_3^+, M_5^+, A_1^-, and R_4^- are found at the special points. The $P4mm$ structure is obtained when the atoms are displaced along the Γ_3^- mode. This structure still has an unstable phonon mode transforming like irrep $X_3(a,b)$, which leads to the $Pmm2$ structure. After relaxing the $Pmm2$ structure, the amplitude of polar distortion Γ_3^- is decreased and the rotational distortion M_3^+ is generated, indicating that these rotational and polar modes compete against each other, as in conventional perovskite oxides [63]. Finally, the unstable phonon mode of the $Pmm2$ structure that transforms like irrep Γ_4 generates the Pm structure. However, this structure is

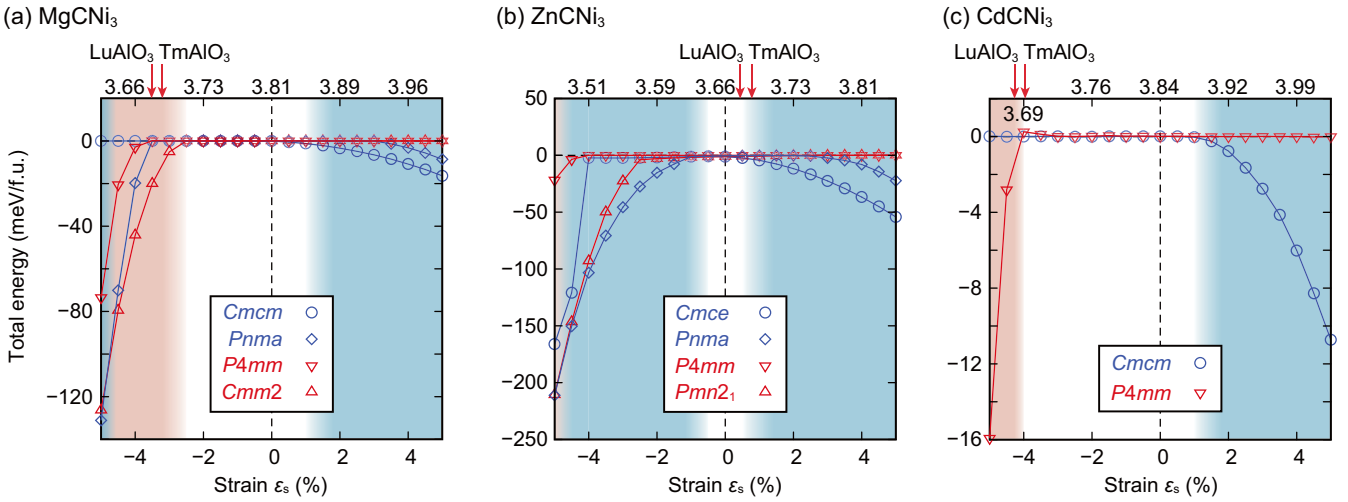

FIG. 5. Total energies of relevant structures for (a) $MgCNi_3$, (b) $ZnCNi_3$, and (c) $CdCNi_3$ as a function of biaxial strain with respect to that of the $P4/mmm$ structure. The lattice constants denoted on the upper horizontal axes are the experimental lattice constants of the $ACNi_3$ $Pm\bar{3}m$ structures times $(1+\epsilon_s)$. Those for the recommended substrates are also indicated by arrows. The energies indicated by red and blue colors are those of polar and antipolar structures, respectively.

relaxed into the dynamically stable higher symmetry $Pmn2_1$ structure. There are five other routes to reach to the $Pmn2_1$ structure, as illustrated in Fig. 4(e). It should be noted that the direction of the polar distortion in the $Pmn2_1$ structure is changed to the [100] axis from the [001] axis by $\Gamma_5^-(a,0)$ from the [001] axis [Fig. 1(c)]. Furthermore, we found one more dynamically stable antipolar $Pnma$ structure (see Table S1 and Fig. S2 of the Supplemental Material [61]). The total energies of the polar $Pmn2_1$ and antipolar $Pnma$ structures are the same within 1 meV/f.u., indicating the difficulty in concluding which is more stable under $\epsilon_s = -5\%$ from our calculations. However, the polar structure is more stabilized upon increasing the compressive strain.

$CdCNi_3$. Two imaginary phonon modes transforming like irreps Γ_3^- and X_2^+ are found. The $P4mm$ structure transforming like irrep Γ_3^- becomes dynamically stable [Fig. 4(f)]. Its total energy compared with that of the parent structure is –16 meV/f.u. Unlike $MgCNi_3$ and $ZnCNi_3$, no antipolar structure is observed in $CdCNi_3$, indicating that antipolar distortion X_2^+ and polar distortion Γ_3^- do not coexist. Therefore, we conclude that the most stable structure in –5% strained $CdCNi_3$ is the polar $P4mm$ structure.

We also confirmed that all the dynamically stable phases in $ACNi_3$ (A = Mg, Zn, and Cd) under strain are nonmagnetic. Moreover, metallic behavior persists in the dynamically stable polar $Cmm2$, $Pmn2_1$, and $P4mm$ structures of $MgCNi_3$, $ZnCNi_3$, and $CdCNi_3$, respectively (see Fig. S3 of the Supplemental Material [61] for their electronic band structures), indicating that they are *polar metals*. The polar-metal phases for $MgCNi_3$ and $CdCNi_3$ are predicted to be the ground states at $-4.5\% < \epsilon_s < -2.8\%$ and $-5.0\% < \epsilon_s < -4.0\%$, respectively, whereas that for $ZnCNi_3$ is metastable [Figs. 5(a)–5(c)].

Although the electronic structures are similar for these three antiperovskites, the structural modulation tendency differs substantially. It is indeed difficult to determine the origin of this difference; however, one reason is likely the difference in the lattice constants. The lattice constants of the $Pm\bar{3}m$ structures in $MgCNi_3$, $ZnCNi_3$, and $CdCNi_3$ are 3.77, 3.72, and 3.81 Å in theory as mentioned above. Another reason could be the difference in the A-atom hybridization with C and Ni [Fig. 3]. For instance, the sign of the Bader charges for Ni atoms changes between $MgCNi_3$ and $A'CNi_3$ (A' = Zn and Cd) [Table II].

To demonstrate the feasibility of the strain-induced polar metals, we compared the total energies of $MgCNi_3$ as a function of strain with those of the experimentally reported strained perovskites $BiFeO_3$ and $EuTiO_3$ [4,5] as shown in Fig. 6. Currently, ±3% strain for epitaxial oxide films is plausible nowadays [2]; in an extreme case, the compressive strain can be as large as –6.6% in $BiFeO_3$ thin films grown on (110) $YAlO_3$ [2]. In Fig. 6, one can see that the strain

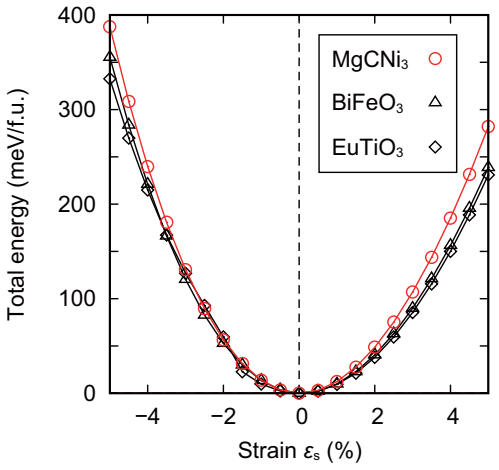

FIG. 6. Total energies of $MgCNi_3$, $BiFeO_3$, $EuTiO_3$ with respect to those of the $Pm\bar{3}m$ structures as a function of epitaxial strain. All the structures were calculated under the $P4/mmm$ symmetry without any octahedral distortion for simplicity. The G-type configurations are considered for Fe and Eu local magnetic moments in $BiFeO_3$ and $EuTiO_3$.

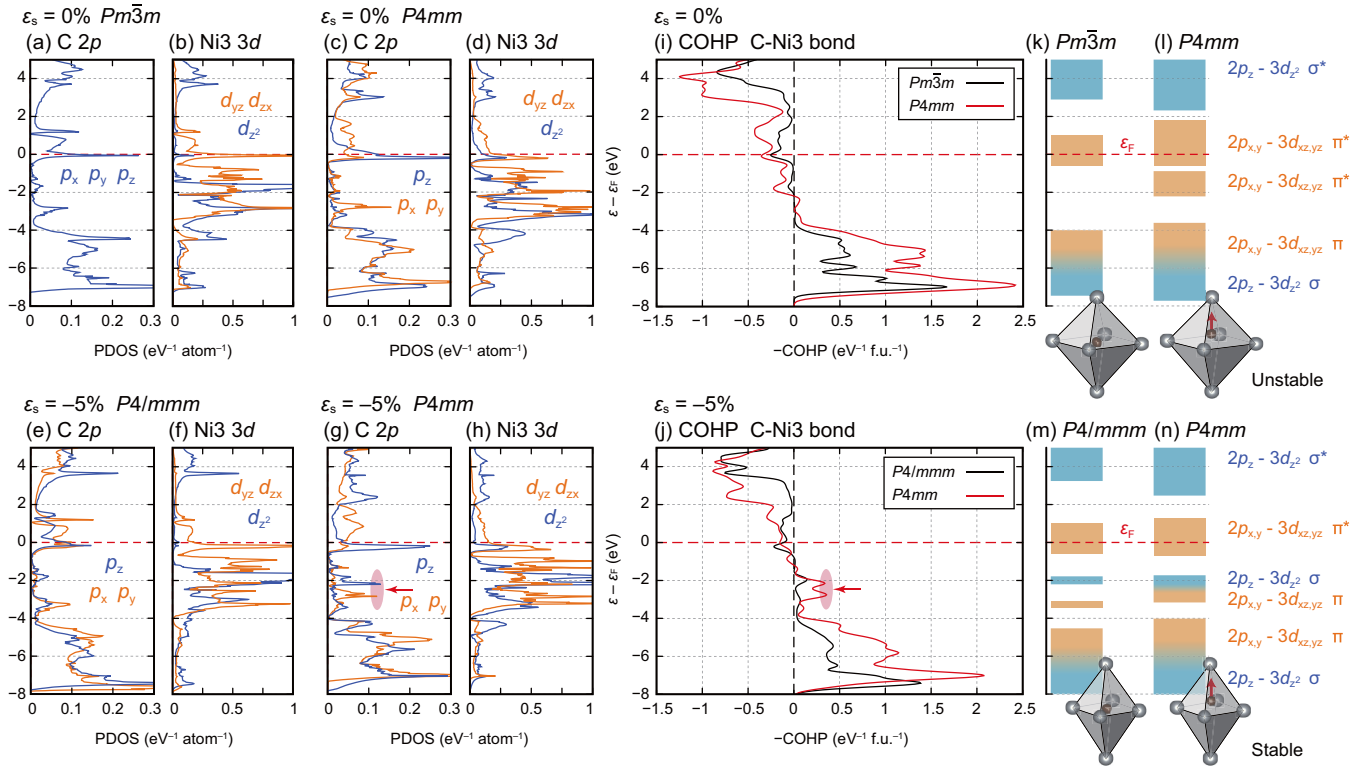

FIG. 7. (a–h) Projected DOS for C $2p$ and Ni $3d$ and (i, j) COHPs for C-Ni3 bondings in the unstrained bulk (a, b, i) $Pm\bar{3}m$ and (c, d, i) $P4mm$ structures and 5% compressively strained (e, f, j) $P4/mmm$ and (g, h, j) $P4mm$ structures of $MgCNi_3$, respectively. The unstrained $P4mm$ structure is artificially constructed by changing the lattice constants of the 5% compressively strained $P4mm$ structure while fixing the atomic fractional coordinates (see text for details). For COHPs, the parent and polar structures are indicated by black and red solid lines, respectively. Note that the horizontal axes in COHPs are denoted with minus signs to follow the convention. (k–n) Schematic energy level diagrams for the unstrained bulk (k) $Pm\bar{3}m$ and (l) $P4mm$ structures as well as 5% compressively strained (m) $P4/mmm$ and (n) $P4mm$ structures. The red arrows and ellipses in (g) PDOS and (j) COHP indicate the emerging bonding in the $P4mm$ structure at $\epsilon_s = -5\%$ between –3 and –2 eV. The blue and orange blurred area in (k–n) indicate the σ and π orbital symmetries, respectively. The atomic positions in the CNi_3 octahedrons are also qualitatively illustrated.

dependence of the total energy of $MgCNi_3$ is comparable to those of $BiFeO_3$ and $EuTiO_3$. Given the experimental achievements on $BiFeO_3$ and $EuTiO_3$, the compressive strain of $-4.5\% < \epsilon_s < -2.8\%$ for polar-metal $MgCNi_3$ should be plausible. The candidate substrates are $LuAlO_3$ and $TmAlO_3$ with the lattice constants of 3.676 and 3.688 Å [64], which apply 3.5% and 3.2% compressive strain to $MgCNi_3$ under ideal epitaxial growth, respectively [Fig. 5(a)].

C. Driving force for polar-metal phases

Metals are thought to have difficulty exhibiting polarity because conduction electrons screen the long-range electrostatic interactions that are key to breaking the inversion symmetry [65–71]. For instance, the conversion of the ferroelectric materials such as $BaTiO_3$, $PbTiO_3$, and $Sr_{1-x}Ca_xTiO_3$ into polar metals by electron doping has been shown to be challenging [68–71]. Indeed, the reported number of polar metals is about 70 according to Ref. [72], and examples include $CeSiPt_3$ [7], Al_3Mg_2 [73], $Cd_2Re_2O_7$ [74], $LiOsO_3$ [65], SnP [75], BeAu [76], epitaxially strained $NdNiO_3$ thin films [66], and tri-layer superlattices $BaTiO_3/SrTiO_3/LaTiO_3$ [77]. Therefore, it is valuable to discuss why polar-metal phases are stabilized in the $ACNi_3$ compounds under compressive strain.

To analyze the electronic structures, the negative-signed COHPs (–COHPs) of the largest interaction between C and apical Ni along the out-of-plane direction (Ni3) were calculated. Figures 7(i) and 7(j) show the –COHPs of $MgCNi_3$ under no strain and 5% compressive strain; those of $ZnCNi_3$ and $CdCNi_3$ are analogous as shown in Figs. S6(a) and S6(b) of the Supplemental Material [61]. The positive (negative) values of –COHP indicate bonding (antibonding) states for the relevant paired atomic orbitals. The schematic energy level diagrams determined in accordance with the –COHPs are presented in Figs. 7(k)–7(n). The contributors near the Fermi level are mostly the π^* orbitals composed of C $2p$ and Ni $3d$ [Figs. 7(a), 7(b), 7(i), and 7(k)] in the unstrained bulk $Pm\bar{3}m$ structure. The π and σ orbitals composed of C $2p$ and Ni $3d$ are located near –5 and –7 eV, respectively, as observed in Figs. 7(a), 7(b), 7(i), and 7(k), which is consistent with a previous report [78].

There are four common features in the three compounds. (i) The largest –COHP originates from the C-Ni bonding in both the unstrained bulk and compressive strain. (ii) By applying compressive strain, the –COHPs for the C-Ni1,2 and A-Ni3 bondings increased, whereas those for C-Ni3 [Figs. 7(i) and 7(j)] and A-Ni1,2 bondings decreased. This tendency is simply due to shrinkage of the C-Ni1,2 and A-Ni3 bond

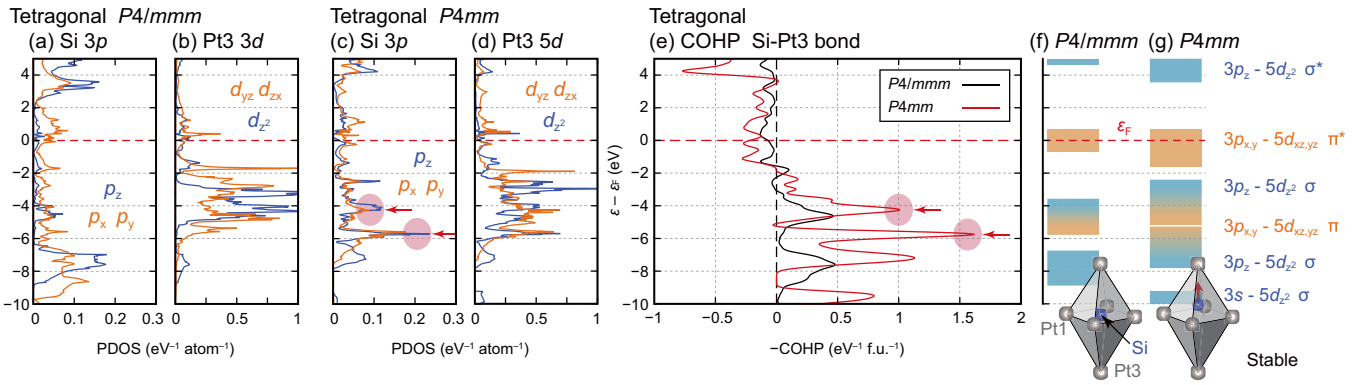

FIG. 8. (a–d) Projected DOS for Si $3p$ and Pt $5d$ and (e) COHPs for Si-Pt3 bondings in the (a, b, e) $P4/mmm$ and (c, d, e) $P4mm$ structures of $CeSiPt_3$. The tetragonal $P4/mmm$ structure is artificially constructed by fixing the in-plane lattice constant at that of the $P4mm$ structure (see text for details). The COHPs are denoted in the same manner as in Fig. 7. The red arrows and ellipses in the (c) PDOS and (e) COHPs indicate the emerging bondings in the $P4mm$ structure near –4 and –6 eV. (f, g) Schematic energy level diagrams for the (f) $P4/mmm$ and (g) $P4mm$ structures. The blue and orange blurred area indicate the σ and π orbitals, respectively. The atomic positions in the $SiPt_3$ octahedrons are also qualitatively illustrated.

lengths and elongation of the C-Ni3 and A-Ni1,2 bond lengths in the $P4/mmm$ structure (see Table S2 of the Supplemental Material [61]). (iii) The –COHPs for C-Ni3 [Fig. 7(j)] and Ni1,2-Ni3 bondings (see Fig. S6(c) of the Supplemental Material [61]) are dramatically increased when the structures are displaced from the $P4/mmm$ to $P4mm$ structures, indicating that the C-Ni3 and Ni1,2-Ni3 interactions are enhanced by the Γ_3^- mode. (iv) The C-Ni3 bonding emerges between -3 and -2 eV in the 5% compressively strained $P4mm$ phase, as highlighted by the red area with arrows in Figs. 7(g) and 7(j). This bonding interaction is likely to be the key factor for stabilizing the polar-metal phases, as further discussed below. The upper (lower) part of the emerging bonding is constructed with mainly C $2p_z$ and Ni $3d_{z^2}$ (C $2p_{x,y}$ and Ni $3d_{xz,yz}$) [Fig. 7(n)].

To verify whether the emerging C-Ni3 bonding is responsible for stabilizing the polar $P4mm$ structure under compressive strain, we calculated the DOS and –COHPs for the artificial unstrained bulk $P4mm$ structure [Figs. 7(c), 7(d) and 7(i)]. This structure was constructed by changing the lattice constants of the $P4mm$ structure at $\epsilon_s = -5\%$ to the unstrained value of $a = 3.77$ Å while fixing the atomic fractional coordinates. It is apparent that the emerging C-Ni3 bonding, which is present between –3 and –2 eV in the $P4mm$ structure at $\epsilon_s = -5\%$, is absent in the unstrained bulk state [Figs. 7(i) and 7(l)]; although C $2p$ states near –3 eV are formed in the unstrained bulk $P4mm$ structure [Fig. 7(c)], they are nonbonding with Ni3 $3d$ states [Fig. 7(i)]. Moreover, the polar distortion in the unstrained bulk $P4mm$ structure increases the COHP of antibonding states near the Fermi level, which results in destabilization of the system, while that in the strained $P4mm$ structure does not increase the COHP. In other words, the compressive strain is indispensable for the emergence of the C-Ni3 bonding.

We direct our discussion back to the Bader charges. By applying compressive strain, the electrons are transferred from C to Ni3 (compare values for the $Pm\bar{3}m$ and $P4/mmm$ (–5%) structures in Table II). In other words, the electron loss of C is triggered by compressive strain. When the structures are displaced from the $P4/mmm$ to $P4mm$ structures by applying the Γ_3^- mode, the electrons at the C and Ni3 sites are increased in such a way as to recover the C charge states. This change most likely results from the creation of C-Ni3 bonding between –3 and –2 eV, as discussed above.

We now compare $ACNi_3$ (A = Mg, Zn, and Cd) with the previously discovered polar metal $CeSiPt_3$ that possesses the same $P4mm$ structure as that of compressively strained $ACNi_3$ [Fig. 8]. The calculated lattice constants are $a = 4.01$ Å, $c = 5.50$ Å, which are comparable to the experimental lattice constants of $a = 4.072$ Å, $c = 5.442$ Å [74]. Because $CeSiPt_3$ takes the polar $P4mm$ structure without strain, we may find an analogy between its unstrained $P4mm$ structure and the strained $P4mm$ structure in $ACNi_3$.

When the structure is changed from the $P4/mmm$ structure to the $P4mm$ structure, strong hybridization between Si and apical Pt along the out-of-plane direction (Pt3) occurs and chemical bonding emerges near –4 and –6 eV [Figs. 8(c), 8(e) and 8(g)], with decreasing Si and Pt3 Bader charges [Table IV]. Although the COHP of the antibonding states near the Fermi level is increased by the polar distortion [Fig. 8(e)], the energy gain by the emerging bonding is much higher; the total energy difference between the $P4mm$ and $P4/mmm$ structures is –6813 meV/f.u. in $CeSiPt_3$. In terms of COHP and Bader charges, the structural change from the $P4/mmm$ to $P4mm$ phases in $CeSiPt_3$ is analogous to those in $ACNi_3$. Thus, the tendency of the charge transfer in $CeSiPt_3$ is qualitatively the same as that in $ACNi_3$. It has been proposed that the driving mechanism of the polar-metal phases in $Cd_2Re_2O_7$ and SnP is a transfer of occupied electrons [74,75]. Therefore,

TABLE IV. Bader charges for $CeSiPt_3$ with the tetragonal $P4/mmm$ and $P4mm$ structures. The apical Pt atoms along the in-plane and out-of-plane direction are denoted as Pt1,2 and Pt3, respectively.

$CeSiPt_3$	Ce	Si	Pt1,2	Pt3
$P4/mmm$	+1.55	+1.92	–1.25	–0.97
$P4mm$	+1.60	+1.27	–0.87	–1.13

some form of charge transfer would be a key to induce polar phases in metals.

A comparison between strained polar metals $ACNi_3$ and electron-doped $BaTiO_3$ may provide insight into the nature of polar metallic behavior. The polar distortion in electron-doped $BaTiO_3$ has been reported to be reduced with increasing carrier electron density in both experimental [67] and theoretical [68,71] studies. This tendency can also be observed in electron-doped $PbTiO_3$ [69] and $Sr_{1-x}Ca_xTiO_3$ [70]. However, Benedek and Birol suggested that the polar structure instability induced by long-range Coulomb interaction is not universal, as this interaction is not a driving force for the polar-metal phase in $LiOsO_3$ [72]. The electron-screening length of the rigid metals such as $CeSiPt_3$ and $ACNi_3$ is extremely short because of their high DOS at the Fermi level. Hence, emerging bonding states below the Fermi level through polar distortions in metals such as $CeSiPt_3$ and strained $ACNi_3$ might be another key to polar phases.

IV. CONCLUSIONS

We explored the ground-state atomic and electronic structures of the epitaxially strained $ACNi_3$ (A = Mg, Zn, and Cd) antiperovskites using first-principles lattice dynamics calculations. Under compressive strain, we found the dynamically stable polar $Cmm2$ and $Pma2$ phases in $MgCNi_3$, $Pmn2_1$ phase in $ZnCNi_3$, and $P4mm$ phase in $CdCNi_3$ as well as the dynamically stable antipolar $Pnma$ phases in $MgCNi_3$ and $ZnCNi_3$ through lattice instabilities. We also demonstrated the feasibility of the strain-induced polar metal $MgCNi_3$ in the compressive strain region of $-4.5\% < \epsilon_s < -2.8\%$. The electron loss of carbon in $ACNi_3$ by the compressive strain is a likely origin of the lattice instability Γ_3^- leading to the $P4mm$ structure. This phase transition is accompanied by enhanced hybridization between C and axial Ni3, and the creation of bonding states a few eV below the Fermi level. Furthermore, the structural change from the $P4/mmm$ to $P4mm$ structures in $ACNi_3$ under compressive strain was shown to be analogous with that in the previously reported polar metal $CeSiPt_3$ without strain. Therefore, the elucidated mechanism is prevalent and could lead to the identification of many more polar metals.

ACKNOWLEDGMENTS

This work was supported by the Japan Society for the Promotion of Science (JSPS) KAKENHI Grants No. JP18J21747 and No. JP17K19172, the Elements Strategy Initiative to Form Core Research Center and the Creation of Life Innovation Materials for Interdisciplinary and International Researcher Development from Ministry of Education, Culture, Sports, Science and Technology (MEXT), and the Support Program for Starting Up Innovation Hub MI^2I from Japan Science and Technology Agency (JST), Japan.

[1] J. M. Rondinelli, S. J. May, and J. W. Freeland, Control of octahedral connectivity in perovskite oxide heterostructures: An emerging route to multifunctional materials discovery, MRS Bull. **37**, 261 (2012).

[2] D. G. Schlom, L.-Q. Chen, C. J. Fennie, V. Gopalan, D. A. Muller, X. Pan, R. Ramesh, and R. Uecker, Elastic strain engineering of ferroic oxides, MRS Bull. **39**, 118 (2014).

[3] J. H. Haeni, P. Irvin, W. Chang, R. Uecker, P. Reiche, Y. L. Li, S. Choudhury, W. Tian, M. E. Hawley, B. Craigo, A. K. Tagantsev, X. Q. Pan, S. K. Streiffer, L. Q. Chen, S. W. Kirchoefer, J. Levy, and D. G. Schlom, Room-temperature ferroelectricity in strained $SrTiO_3$, Nature **430**, 758 (2004).

[4] J. Wang, J. B. Neaton, H. Zheng, V. Nagarajan, S. B. Ogale, B. Liu, D. Viehland, V. Vaithyanathan, D. G. Schlom, U. V. Waghmare, N. A. Spaldin, K. M. Rabe, M. Wuttig, and R. Ramesh, Epitaxial $BiFeO_3$ multiferroic thin film heterostructures, Science **299**, 1719 (2003).

[5] J. H. Lee, L. Fang, E. Vlahos, X. Ke, Y. W. Jung, L. F. Kourkoutis, J.-W. Kim, P. J. Ryan, T. Heeg, M. Roeckerath, V. Goian, M. Bernhagen, R. Uecker, P. C. Hammel, K. M. Rabe, S. Kamba, J. Schubert, J. W. Freeland, D. A. Muller, C. J. Fennie, P. Schiffer, V. Gopalan, E. Johnston-Halperin, and D. G. Schlom, A strong ferroelectric ferromagnet created by means of spin–lattice coupling, Nature **466**, 954 (2010).

[6] R. Ramesh and N. A. Spaldin, Multiferroics: Progress and prospects in thin films, Nat. Mater. **6**, 21 (2007).

[7] E. Bauer, G. Hilscher, H. Michor, C. Paul, E. W. Scheidt, A. Gribanov, Y. Seropegin, H. Noël, M. Sigrist, and P. Rogl, Heavy Fermion Superconductivity and Magnetic Order in Noncentrosymmetric $CePt_3Si$, Phys. Rev. Lett. **92**, 027003 (2004).

[8] T. He, Q. Huang, A. P. Ramirez, Y. Wang, K. A. Regan, N. Rogado, M. A. Hayward, M. K. Haas, J. S. Slusky, K. Inumara, H. W. Zandbergen, N. P. Ong, and R. J. Cava, Superconductivity in the nonoxide perovskite $MgCNi_3$, Nature **411**, 54 (2001).

[9] M. Uehara, T. Yamazaki, T. Kori, T. Kashida, Y. Kimishima, and I. Hase, Superconducting properties of $CdCNi_3$, J. Phys. Soc. Jpn. **76**, 034714 (2007).

[10] M. Uehara, A. Uehara, K. Kozawa, and Y. Kimishima, New antiperovskite-type superconductor ZnN_yNi_3, J. Phys. Soc. Jpn. **78**, 033702 (2009).

[11] B. He, C. Dong, L. Yang, X. Chen, L. Ge, L. Mu, and Y. Shi, $CuNNi_3$: A new nitride superconductor with antiperovskite structure, Supercond. Sci. Technol. **26**, 125015 (2013).

[12] M. Oudah, A. Ikeda, J. N. Hausmann, S. Yonezawa, T. Fukumoto, S. Kobayashi, M. Sato, and Y. Maeno, Superconductivity in the antiperovskite Dirac-metal oxide $Sr_{3-x}SnO$, Nat. Commun. **7**, 13617 (2016).

[13] K. Kamishima, T. Goto, H. Nakagawa, N. Miura, M. Ohashi, N. Mori, T. Sasaki, and T. Kanomata, Giant magnetoresistance in the intermetallic compound Mn_3GaC, Phys. Rev. B **63**, 024426 (2000).

[14] K. Asano, K. Koyama, and K. Takenaka, Magnetostriction in Mn_3CuN, Appl. Phys. Lett. **92**, 161909 (2008).

[15] S. Iikubo, K. Kodama, K. Takenaka, H. Takagi, M. Takigawa, and S. Shamoto, Local Lattice Distortion in the Giant Negative Thermal Expansion Material $Mn_3Cu_{1-x}Ge_xN$, Phys. Rev. Lett. **101**, 205901 (2008).

[16] Y. Sun, X.-Q. Chen, S. Yunoki, D. Li, and Y. Li, New Family of Three-Dimensional Topological Insulators with Antiperovskite Structure, Phys. Rev. Lett. **105**, 216406 (2010).

[17] R. Yu, H. Weng, Z. Fang, X. Dai, and X. Hu, Topological Node-Line Semimetal and Dirac Semimetal State in Antiperovskite Cu_3 PdN, Phys. Rev. Lett. **115**, 036807 (2015).

[18] Y. Obata, R. Yukawa, K. Horiba, H. Kumigashira, Y. Toda, S. Matsuishi, and H. Hosono, ARPES studies of the inverse perovskite Ca_3 PbO: Experimental confirmation of a candidate 3D Dirac fermion system, Phys. Rev. B **96**, 155109 (2017).

[19] D. Samal, H. Nakamura, and H. Takagi, Molecular beam epitaxy of three-dimensional Dirac material Sr_3 PbO, APL Mater. **4**, 076101 (2016).

[20] Z. Hui, X. Tang, D. Shao, R. Wei, J. Yang, P. Tong, W. Song, X. Zhu, and Y. Sun, Self-assembled c-axis oriented antiperovskite soft-magnetic $CuNCo_3$ thin films by chemical solution deposition, J. Mater. Chem. C **3**, 4438 (2015).

[21] Z. Hui, X. Tang, D. Shao, H. Lei, J. Yang, W. Song, H. Luo, X. Zhu, and Y. Sun, Epitaxial antiperovskite superconducting $CuNNi_3$ thin films synthesized by chemical solution deposition, Chem. Commun. **50**, 12734 (2014).

[22] Y. F. Lee, F. Wu, R. Kumar, F. Hunte, J. Schwartz, and J. Narayan, Epitaxial integration of dilute magnetic semiconductor Sr_3 SnO with Si (001), Appl. Phys. Lett. **103**, 112101 (2013).

[23] M.-S. Park, J. Giim, S.-H. Park, Y. W. Lee, S. I. Lee, and E. J. Choi, Physical properties of $ZnCNi_3$: Comparison with superconducting $MgCNi_3$, Supercond. Sci. Technol. **17**, 274 (2004).

[24] A. Dong, G. Che, W. Huang, S. Jia, H. Chen, and Z. Zhao, Synthesis and physical properties of $AlCNi_3$, Physica C **422**, 65 (2005).

[25] P. Tong, Y. P. Sun, X. B. Zhu, and W. H. Song, Strong electron-electron correlation in the antiperovskite compound $GaCNi_3$, Phys. Rev. B **73**, 245106 (2006).

[26] P. Tong, Y. Sun, X. Zhu, and W. Song, Synthesis and physical properties of antiperovskite-type compound $In_{0.95}CNi_3$, Solid State Commun. **141**, 336 (2007).

[27] M. Uehara, A. Uehara, K. Kozawa, T. Yamazaki, and Y. Kimishima, New antiperovskite superconductor $ZnNNi_3$, and related compounds $CdNNi_3$ and $InNNi_3$, Physica C **470**, S688 (2010).

[28] T. Ideue, K. Hamamoto, S. Koshikawa, M. Ezawa, S. Shimizu, Y. Kaneko, Y. Tokura, N. Nagaosa, and Y. Iwasa, Bulk rectification effect in a polar semiconductor, Nat. Phys. **13**, 578 (2017).

[29] T. Morimoto and N. Nagaosa, Nonreciprocal current from electron interactions in noncentrosymmetric crystals: Roles of time reversal symmetry and dissipation, Sci. Rep. **8**, 2973 (2018).

[30] B. S. Wang, P. Tong, Y. P. Sun, X. Luo, X. B. Zhu, G. Li, X. D. Zhu, S. B. Zhang, Z. R. Yang, W. H. Song, and J. M. Dai, Large magnetic entropy change near room temperature in antiperovskite $SnCMn_3$, Europhys. Lett. **85**, 47004 (2009).

[31] E. Chi, W. Kim, and N. Hur, Nearly zero temperature coefficient of resistivity in antiperovskite compound $CuNMn_3$, Solid State Commun. **120**, 307 (2001).

[32] W. S. Kim, E. O. Chi, J. C. Kim, N. H. Hur, K. W. Lee, and Y. N. Choi, Cracks induced by magnetic ordering in the antiperovskite $ZnNMn_3$, Phys. Rev. B **68**, 172402 (2003).

[33] C. Höglund, J. Birch, M. Beckers, B. Alling, Z. Czigány, A. Mücklich, and L. Hultman, Sc_3 AlN - A new perovskite, Eur. J. Inorganic Chem. **2008**, 1193 (2008).

[34] M. Kirchner, W. Schnelle, F. R. Wagner, and R. Niewa, Preparation, crystal structure and physical properties of ternary compounds (R_3N)In, R = rare-earth metal, Solid State Sciences **5**, 1247 (2003).

[35] E. Chi, W. Kim, N. Hur, and D. Jung, New Mg-based antiperovskites $PnNMg_3$ (Pn = As, Sb), Solid State Commun. **121**, 309 (2002).

[36] M. Y. Chern, D. Vennos, and F. Disalvo, Synthesis, structure, and properties of antiperovskite nitrides Ca_3 MN, M = P, As, Sb, Bi, Ge, Sn, and Pb, J. Solid State Chem. **96**, 415 (1992).

[37] M. Y. Chern, F. Disalvo, J. Parise, and J. A. Goldstone, The structural distortion of the antiperovskite nitride Ca_3 AsN, J. Solid State Chem. **96**, 426 (1992).

[38] F. Gäbler, M. Kirchner, W. Schnelle, U. Schwarz, M. Schmitt, H. Rosner, and R. Niewa, $(Sr_3N)E$ and $(Ba_3N)E$ (E = Sb, Bi): Synthesis, crystal structures, and physical properties, Z. Anorg. Allg. Chem. **630**, 2292 (2004).

[39] Y. Okamoto, A. Sakamaki, and K. Takenaka, Thermoelectric properties of antiperovskite calcium oxides Ca_3PbO and Ca_3SnO, J. Appl. Phys. **119**, 205106 (2016).

[40] P. E. Blöchl, Projector augmented-wave method, Phys. Rev. B **50**, 17953 (1994).

[41] J. P. Perdew, A. Ruzsinszky, G. I. Csonka, O. A. Vydrov, G. E. Scuseria, L. A. Constantin, X. Zhou, and K. Burke, Restoring the Density-Gradient Expansion for Exchange in Solids and Surfaces, Phys. Rev. Lett. **100**, 136406 (2008).

[42] G. Kresse and J. Furthmüller, Efficient iterative schemes for *ab initio* total-energy calculations using a plane-wave basis set, Phys. Rev. B **54**, 11169 (1996).

[43] G. Kresse and D. Joubert, From ultrasoft pseudopotentials to the projector augmented-wave method, Phys. Rev. B **59**, 1758 (1999).

[44] S. L. Dudarev, G. A. Botton, S. Y. Savrasov, C. J. Humphreys, and A. P. Sutton, Electron-energy-loss spectra and the structural stability of nickel oxide: An LSDA+U study, Phys. Rev. B **57**, 1505 (1998).

[45] A. Togo and I. Tanaka, First-principles phonon calculations in materials science, Scr. Mater. **108**, 1 (2015).

[46] A. Togo, F. Oba, and I. Tanaka, Transition pathway of CO_2 crystals under high pressures, Phys. Rev. B **77**, 184101 (2008).

[47] A. Togo and I. Tanaka, Evolution of crystal structures in metallic elements, Phys. Rev. B **87**, 184104 (2013).

[48] H. Akamatsu, K. Fujita, T. Kuge, A. Sen Gupta, A. Togo, S. Lei, F. Xue, G. Stone, J. M. Rondinelli, L.-Q. Chen, I. Tanaka, V. Gopalan, and K. Tanaka, Inversion Symmetry Breaking by Oxygen Octahedral Rotations in the Ruddlesden-Popper $NaRTiO_4$ Family, Phys. Rev. Lett. **112**, 187602 (2014).

[49] D. Orobengoa, C. Capillas, M. I. Aroyo, and J. M. Perez-Mato, AMPLIMODES: Symmetry-mode analysis on the bilbao crystallographic server, J. Appl. Crystallogr. **42**, 820 (2009).

[50] J. M. Perez-Mato, D. Orobengoa, and M. I. Aroyo, Mode crystallography of distorted structures, Acta Crystallogr. Sect. A **66**, 558 (2010).

[51] R. Dronskowski and P. E. Blöchl, Crystal orbital Hamilton populations (COHP): Energy-resolved visualization of chemical bonding in solids based on density-functional calculations, J. Phys. Chem. **97**, 8617 (1993).

[52] V. L. Deringer, A. L. Tchougréeff, and R. Dronskowski, Crystal orbital Hamilton population (COHP) analysis as projected from plane-wave basis sets, J. Phys. Chem. A **115**, 5461 (2011).

[53] S. Maintz, V. L. Deringer, A. L. Tchougreeff, and R. Dronskowski, Analytic projection from plane-wave and PAW wavefunctions and application to chemical-bonding analysis in solids, J. Comput. Chem. **34**, 2557 (2013).

[54] S. Maintz, V. L. Deringer, A. L. Tchougréeff, and R. Dronskowski, LOBSTER: A tool to extract chemical bonding from plane-wave based DFT, J. Comput. Chem. **37**, 1030 (2016).

[55] S. Maintz, M. Esser, and R. Dronskowski, Efficient rotation of local basis functions using real spherical harmonics, Acta Phys. Pol. B **47**, 1165 (2016).

[56] W. Tang, E. Sanville, and G. Henkelman, A grid-based bader analysis algorithm without lattice bias, J. Phys.: Condens. Matter **21**, 084204 (2009).

[57] E. Sanville, S. D. Kenny, R. Smith, and G. Henkelman, Improved grid-based algorithm for Bader charge allocation, J. Comput. Chem. **28**, 899 (2007).

[58] G. Henkelman, A. Arnaldsson, and H. Jonsson, A fast and robust algorithm for Bader decomposition of charge density, Comput. Mater. Sci. **36**, 354 (2006).

[59] M. Yu and D. R. Trinkle, Accurate and efficient algorithm for Bader charge integration, J. Chem. Phys. **134**, 064111 (2011).

[60] J. C. Slater, Atomic radii in crystals, J. Chem. Phys. **41**, 3199 (1964).

[61] See Supplemental Material at http://link.aps.org/supplemental/10.1103/PhysRevMaterials.2.125004 for the details of the schematics for the structural distortions, phonon band structures, and treelike line diagrams under 5% tensile strain, the bond lengths and electronic structures for the unstrained bulk $Pm\bar{3}m$ structures, compressively strained $P4/mmm$ and $P4mm$ structures of $ACNi_3$ (A = Mg, Zn, and Cd), and COHPs for C-Ni3 bonding in $ZnCNi_3$ and $CdCNi_3$.

[62] L. Pauling, The nature of the chemical bond. IV. The energy of single bonds and the relative electronegativity of atoms, J. Am. Chem. Soc. **54**, 3570 (1932).

[63] N. A. Benedek and C. J. Fennie, Why are there so few perovskite ferroelectrics? J. Phys. Chem. C **117**, 13339 (2013).

[64] T. Shishido, S. Nojima, M. Tanaka, H. Horiuchi, and T. Fukuda, Flux growth of perovskite-type $RAlO_3$ single crystals, J. Alloys Compd. **227**, 175 (1995).

[65] Y. Shi, Y. Guo, X. Wang, A. J. Princep, D. Khalyavin, P. Manuel, Y. Michiue, A. Sato, K. Tsuda, S. Yu, M. Arai, Y. Shirako, M. Akaogi, N. Wang, K. Yamaura, and A. T. Boothroyd, A ferroelectric-like structural transition in a metal, Nat. Mater. **12**, 1024 (2013).

[66] T. H. Kim, D. Puggioni, Y. Yuan, L. Xie, H. Zhou, N. Campbell, P. J. Ryan, Y. Choi, J. W. Kim, J. R. Patzner, S. Ryu, J. P. Podkaminer, J. Irwin, Y. Ma, C. J. Fennie, M. S. Rzchowski, X. Q. Pan, V. Gopalan, J. M. Rondinelli, and C. B. Eom, Polar metals by geometric design, Nature **533**, 68 (2016).

[67] T. Kolodiazhnyi, M. Tachibana, H. Kawaji, J. Hwang, and E. Takayama-Muromachi, Persistence of Ferroelectricity in $BaTiO_3$ Through the Insulator-Metal Transition, Phys. Rev. Lett. **104**, 147602 (2010).

[68] Y. Iwazaki, T. Suzuki, Y. Mizuno, and S. Tsuneyuki, Doping-induced phase transitions in ferroelectric $BaTiO_3$ from first-principles calculations, Phys. Rev. B **86**, 214103 (2012).

[69] X. He and K.-j. Jin, Persistence of polar distortion with electron doping in lone-pair driven ferroelectrics, Phys. Rev. B **94**, 224107 (2016).

[70] C. W. Rischau, X. Lin, C. P. Grams, D. Finck, S. Harms, J. Engelmayer, T. Lorenz, Y. Gallais, B. Fauqué, J. Hemberger, and K. Behnia, A ferroelectric quantum phase transition inside the superconducting dome of $Sr_{1-x}Ca_xTiO_{3-\delta}$, Nat. Phys. **13**, 643 (2017).

[71] Y. Wang, X. Liu, J. D. Burton, S. S. Jaswal, and E. Y. Tsymbal, Ferroelectric Instability Under Screened Coulomb Interactions, Phys. Rev. Lett. **109**, 247601 (2012).

[72] N. A. Benedek and T. Birol, "Ferroelectric" metals reexamined: Fundamental mechanisms and design considerations for new materials, J. Mater. Chem. C **4**, 4000 (2016).

[73] E. Bauer, H. Kaldarar, R. Lackner, H. Michor, W. Steiner, E.-W. Scheidt, A. Galatanu, F. Marabelli, T. Wazumi, K. Kumagai, and M. Feuerbacher, Superconductivity in the complex metallic alloy $\beta-Al_3Mg_2$, Phys. Rev. B **76**, 014528 (2007).

[74] I. A. Sergienko, V. Keppens, M. McGuire, R. Jin, J. He, S. H. Curnoe, B. C. Sales, P. Blaha, D. J. Singh, K. Schwarz, and D. Mandrus, Metallic "Ferroelectricity" in the Pyrochlore $Cd_2Re_2O_7$, Phys. Rev. Lett. **92**, 065501 (2004).

[75] M. Kamitani, M. S. Bahramy, T. Nakajima, C. Terakura, D. Hashizume, T. Arima, and Y. Tokura, Superconductivity at the Polar-Nonpolar Phase Boundary of SnP with an Unusual Valence State, Phys. Rev. Lett. **119**, 207001 (2017).

[76] A. Amon, E. Svanidze, R. Cardoso-Gil, M. N. Wilson, H. Rosner, M. Bobnar, W. Schnelle, J. W. Lynn, R. Gumeniuk, C. Hennig, G. M. Luke, H. Borrmann, A. Leithe-Jasper, and Y. Grin, Noncentrosymmetric superconductor BeAu, Phys. Rev. B **97**, 014501 (2018).

[77] Y. Cao, Z. Wang, S. Y. Park, Y. Yuan, X. Liu, S. M. Nikitin, H. Akamatsu, M. Kareev, S. Middey, D. Meyers, P. Thompson, P. J. Ryan, P. Shafer, A. N'Diaye, E. Arenholz, V. Gopalan, Y. Zhu, K. M. Rabe, and J. Chakhalian, Artificial two-dimensional polar metal at room temperature, Nat. Commun. **9**, 1547 (2018).

[78] J. H. Shim, S. K. Kwon, and B. I. Min, Electronic structures of antiperovskite superconductors $MgXNi_3$ (X = B, C, and N), Phys. Rev. B **64**, 180510 (2001).